Journal of Materials Chemistry B

ROYAL SOCIETY OF CHEMISTRY

PAPER

View Article Online
View Journal

Cite this: DOI: 10.1039/c9tb02102g

Photo-induced synthesis of molybdenum oxide quantum dots for surface-enhanced Raman scattering and photothermal therapy†

Haihong Yu,‡[a] Zhengfei Zhuang,‡[a] Dongling Li,[a] Yanxian Guo,[a] Yang Li,[a] Huiqing Zhong,[a] Honglian Xiong,[b] Zhiming Liu *[a] and Zhouyi Guo *[a]

Received 26th September 2019,
Accepted 4th December 2019

DOI: 10.1039/c9tb02102g

rsc.li/materials-b

By means of a simple and photo-induced method, four colors of molybdenum oxide quantum dots (MoO_x QDs) have been synthesized, using $Mo(CO)_6$ as the structural guiding agent and molybdenum source. The as-prepared MoO_x QDs display diverse optical properties due to the different configurations of oxygen vacancies in various nanostructures. Among them, crystalline molybdenum dioxide (MoO_2) with a deep blue color shows the most intense localized surface plasmon resonance effect in the near-infrared (NIR) region. The strong NIR absorption endows MoO_2 QDs with a high photothermal conversion efficiency of 66.3%, enabling broad prospects as a photo-responsive nanoagent for photothermal therapy of cancer. Moreover, MoO_2 QDs can also serve as a novel semiconductor substrate for ultrasensitive surface-enhanced Raman scattering (SERS) analysis of aromatic molecules, amino acids and antibiotics, with SERS performance comparable to that of noble metal-based substrates. The therapeutic applications of MoO_2 QDs open up a new avenue for tumor nanomedicine.

Introduction

Flake-like two-dimensional (2D) nanomaterials have captured substantial attention for their favorable light–matter interactions in a wide range from ultraviolet (UV) to near-infrared (NIR) regions since the discovery of graphene, black phosphorus (BP) and their derivatives.[1] The utilization of 2D nanostructures as promising photo-responsive nanoprobes for optical imaging, molecular sensing and phototherapy has been exploited prevalently in recent years.[2,3] For biomedical applications, the light-responsive features of nanomaterials in the NIR region (also named as the ''biological transparency window'') are advantageous, which however poses a dilemma to graphene- or BP-based nanostructures. More recently, plasmonic 2D materials have received great interest because of their appreciable localized surface plasmon resonance (LSPR) effect derived from the collective oscillations of valence electrons in the nanostructures under illumination.[4,5]

As a star member of the transition metal oxides (TMOs), molybdenum oxide (MoO_x) provides a plasmonic resonance from visible to NIR wavelengths. The morphology and size of MoO_x nanostructures, including nanoparticles, nanodumbbels, nanoclusters, 2D nanosheets (NSs) and their 0D derivatives, and quantum dots (QDs), can be easily modulated *via* intelligent synthesis strategies.[6–11] It is well known that biodegradability is one of the critical parameters for clinical translation of a nanomaterial.[12] MoO_x is biodegradable, which has been discussed in several papers.[7,13,14] MoO_x NSs show a pH-responsive degradation property. The nanosheets are relatively stable at acidic pH while being degradable at physiological pH, which leads to longer tumor retention of those nanosheets but little influence on normal tissues.[13] More interestingly, the LSPR peak of MoO_x is tunable by controlling the concentration of oxygen vacancy in the lattices,[15] making MoO_x an efficient NIR-responsive nanomaterial for diverse optical applications.[16–18] For example, Song *et al.* described a hydrothermal strategy for fabricating biodegradable MoO_x NSs using ammonium molybdate as the Mo source.[8] The 2D semiconductor showed good capabilities as a NIR nanoprobe for tumor photoacoustic imaging and photothermal therapy (PTT) with rapid body clearance. MoO_x QDs can also be prepared by the hydrothermal method. In a study conducted by Liu *et al.*, molybdenum powder was chosen as a precursor for the preparation of MoO_x QDs with size around 2.5 nm, which displayed strong NIR harvesting ability to convert NIR lasers into hyperthermia for cancer theranostics.[19]

[a] MOE Key Laboratory of Laser Life Science & SATCM Third Grade Laboratory of Chinese Medicine and Photonics Technology, College of Biophotonics, South China Normal University, Guangzhou, Guangdong 510631, P. R. China. E-mail: liuzm021@126.com, ann@scnu.edu.cn

[b] Department of Physics and Optoelectronic Engineering, Foshan University, Guangdong, P. R. China

† Electronic supplementary information (ESI) available. See DOI: 10.1039/c9tb02102g

‡ These authors contributed equally to the work.

In addition, the LSPR effect will lead to an electromagnetic enhancement in Raman scattering.[20] In fact, many efforts have been made to exploit novel surface-enhanced Raman scattering (SERS) substrates based on semiconductor materials in recent years, especially plasmonic TMOs.[21] Compared to the traditional SERS substrates composed of noble metals (*e.g.*, Au and Ag), TMOs are cheaper, more versatile and have better biocompatibility. Furthermore, the Raman enhancement induced by plasmonic TMOs has proven to be comparable to noble metals, and the SERS effect is largely dependent on the density of d-orbital free electrons in the oxygen vacancies.[22] This is evident in dumbbell-like MoO_x nanostructures reported by Zhang *et al.*, where the MoO_2 nanodumbbells without a LSPR band showed almost no SERS effect on R6G molecules, while remarkable Raman enhancement was achieved using their plasmonic counterparts as the SERS substrates.[9] The Raman enhancement factor (EF) and the limit of detection (LOD) of plasmonic MoO_2 reached 3.75×10^6 and 10^{-7} M, respectively. Another striking example is 2D MoO_2 NSs whose LOD and EF were observed to be 4×10^{-8} M and 2.1×10^5, respectively.[23] Li *et al.* also reported that amorphous MoO3 QDs synthesized from MoS_2 powder with the assistance of supercritical CO_2 presented a superior EF of methyl blue (MB) molecules of up to 9.5×10^5.[24] It should be noted that the Raman tests in the current work were mostly carried out on dried samples, while liquid-phase Raman analysis is rarely performed.

There are many ways to synthesize molybdenum oxides, such as the hydrothermal method,[7,8,25,26] laser ablation,[27] chemical vapor deposition,[28] the supercritical CO_2 assisted method,[24] and so on. Most of the synthetic methods require high temperature, high pressure, femtosecond lasers, etchants, *etc.*, which are operationally hazardous, energy extravagant and environment-unfriendly. Therefore, safe, low pollution, energy-saving and controllable synthesis methods urgently need to be exploited. Herein, a simple photo-induced method for preparing plasmonic MoO_x QDs is proposed using molybdenum hexacarbonyl ($Mo(CO)_6$) as the molybdenum source, by means of which four varieties of MoO_x QDs are obtained. The plasmonic nanostructures and oxygen vacancy defects in the MoO_x QDs can be controlled by the light irradiation dose. The optimal LSPR feature of the MoO_x QDs can be observed when the molybdenum precursor underwent sunlight irradiation for 10 h, namely MoO_2 QDs. The NIR-responsive feature allows the MoO_2 QDs to act as photothermal nanoagents for high-performance cancer PTT. Liquid-phase SERS analysis of dye molecules is also performed using MoO_2 QDs as ultrasensitive SERS substrates, wherein the LOD and the maximum EF of MB in solution are about 10^{-8} M and 7×10^6, respectively. Furthermore, the SERS detection of phenylalanine and amphotericin B is also achieved, indicating the promising potential of MoO_2 QDs for bioanalysis.

Experimental

Materials

Methylene blue (MB), malachite green (MG), and calcium chloride ($CaCl_2$) were purchased from Sigma-Aldrich. Hexacarbonylmolybdenum (Mo(CO)6) was purchased from Yuanye Biotechnology (Shanghai, China). *N*,*N*-Dimethylformamide was obtained from Aladdin (Shanghai, China). Dulbecco's modified Eagle's medium (DMEM) and fetal bovine serum (FBS) were purchased from GIBCO (Grand Island, NY, USA). The Annexin V-FITC-PI Apoptosis Detection Kit was purchased from Dalian Meilun (Liaoning, China). All reagents were used without further purification. Deionized water (Milli-Q System, Millipore, USA) was used in all experiments.

Synthesis of molybdenum oxide quantum dots

Preparation of reduced state molybdenum quantum dots: a general fabrication process is as follows: first, 1 mM $Mo(CO)_6$ was dispersed into dimethyl formamide and sonicated for 30 min. In the presence of a flow of nitrogen, the mixed solution was added into a three necked flask and heated to 80 °C for 1 h under magnetic stirring. During this process, the color of the solution changed from colorless to yellowish-brown. When cooled to room temperature, the yellow intermediate was moved into an ultra-low temperature freeze dryer for 12 h. Excess ethanol was added to wash the products and a dry yellow solid was obtained by freeze drying.

Synthesis of molybdenum oxide quantum dots with different degrees of oxidation: the initial yellow intermediate (0.4 mg) was dispersed into 50% ethanol solution (10 mL). After sonicating for 30 min, the mixed solution was put in sunlight ($\sim$0.2 mW cm^{-2}) for 2 h to get a light green product (G). At 5 h, the colour changed to light blue, which meant the formation of B. At 10 h, DB was acquired with the colour of the solution turning dark blue. If the yellow mixed 50% ethanol aqueous solution was put under a UV lamp for 5 h, G_2 was synthesized (green color).

Coating of calcium carbonate

$CaCl_2{\cdot}2H_2O$ (20 mg) and MoO_2 (40 μL, 10 mg mL^{-1}) were dispersed in a beaker containing 10 mL of ethanol solution, which was adjusted to pH 6.8 and sealed with a plastic wrap to form a number of pores. The bottle was then placed in a desiccator with two bottles of amino bicarbonate (NH4HCO3) at a temperature of 45 °C. After 1 day of vapor diffusion reaction, the product was centrifuged and collected at 12 000 rpm for 20 min.

Characterization

Transmission electron microscopy (TEM) images were obtained on a 200 kV JEM-2100HR transmission electron microscope (JEOL, Japan) equipped with an EDX spectrometer. UV-vis-NIR absorption spectra were collected on a spectrophotometer (UV-6100S, MAPADA, China). The X-ray diffraction (XRD) pattern was obtained using a Bruker D8 focus X-ray diffractometer under CuKα radiation (λ = 1.54051 Å). Raman spectra were measured by a Renishaw inVia microspectrometer (Derbyshire, England) equipped with an excitation wavelength of 785 nm. XPS spectra were measured by using a Thermo Fisher Scientific K-Alpha photoelectron spectrometer (Shanghai, China). Apoptosis assay was performed *via* ACEA NovoCyteTM Flow Cytometry (San Diego, USA).

Raman measurement

Different kinds of aqueous dye solutions with concentrations varying from 10^{-3} to 10^{-8} M were mixed with equivalent MoO_x QDs (1 mg mL^{-1}). Next, 4 μL of suspension was extracted and dropped onto a cleaned silicon wafer for Raman scanning. The Raman spectrum was obtained by using a high-resolution confocal Raman spectrometer (Derbyshire, England) at the excitation wavelength of 785 nm with the laser power of 0.5 mW. A 20× objective lens was used to focus the sample. All the samples were measured at least six times and the EFs were calculated as follows:

$$EF = I_{SERS} \times C_{Raman}/I_{Raman} \times C_{SERS} \quad (1)$$

where I_{SERS} represents the SERS signal caused by the concentration of probe molecules (C_{SERS}), and I_{Raman} refers to the normal Raman signal obtained due to the concentration of probe molecules (C_{Raman}).

Photothermal properties of MoO_x QDs

The temperature changes of MoO_x QD solutions (0–100 μg mL^{-1}) under 808 nm laser irradiation (0.33, 1 and 2 W cm^2) were measured by an infrared thermal camera (Fluke Ti200, FlukeCorp, Washington, USA). The temperature was recorded every 30 s for 10 min. The photothermal conversion efficiency (η) was estimated using the equation below:[47]

$$\eta = hs(T_{max} - T_{max,water})/I(1 - 10^{-A}) \quad (2)$$

$$hs = \Sigma mC_p/\tau_S \quad (3)$$

$$\tau_S = -t/\ln\theta \quad (4)$$

$$\theta = (T_{amb} - T)/(T_{amb} - T_{max}) \quad (5)$$

where h represents the heat conversion coefficient and s denotes the surface area of the container. Here, τ_S represents the system time constant of the sample, and m and C_p represent the mass (1 g) and specific heat capacity of the solvent ($C_{p,water}$ = 4.2 J g^{-1}), respectively. T_{amb} is the ambient temperature of the surroundings, and T_{max} and $T_{max,water}$ are the equilibrium temperatures of the MoO_2 solution and water, respectively. I is the laser power density (2 W cm^{-2}), and A represents the absorbance of MoO_2 solution at 808 nm (A_{808} = 0.294).

In vitro photothermal cancer therapy

Hep G2 cells were obtained from the Laboratory Animal Center of Sun Yat-sen University (China) and cultured in DMEM (Gibco, USA) supplemented with 10% fetal bovine serum (FBS) and 1% penicillin/streptomycin at 37 °C in a humidified atmosphere with 5% CO_2 till the desired confluency was achieved. The standard tetrazolium salt (MTT) assay was performed to determine the cell viability. Briefly, Hep G2 cells were seeded in 96-well plates with a density of 10^4 cells per well and incubated in a CO_2 incubator for 12 h at 37 °C. Then, the medium was displaced by fresh medium containing various concentrations of the MoO_2 QDs. The cells were cultured in a CO_2 incubator for 24 h. Subsequently, MTT (5 mg mL^{-1}) was added to each well for 4 h at 37 °C. Then, the medium was replaced by DMSO, and the absorbance at 495 nm was measured using a microplate reader.

Hep G2 cells were seeded into 6-well culture plates (about 5×10^4 cells per well), followed by incubation with MoO_2 QDs (100 μg mL^{-1}) or PBS for 8 h. Finally, the Hep G2 cells were irradiated with an 808 nm laser at the power density of 2 W cm^{-2} for 2.5 min. Subsequently, the cells were stained with calcein AM/PI for 15 minutes, and imaged by a fluorescence microscope (Calcein AM lex = 488 nm, lem = 515 nm; PI lex = 535 nm, lem = 617 nm).

Apoptosis assay was performed using the Annexin-V-FITC-PI apoptosis detection kit (Meilun, Dalian, China). Briefly, 5 μL of annexin-V-FITC and 5 μL of PI solution were added to 100 μL of cell suspension (1×10^5). Cells were incubated in the dark for 15 minutes at 25 °C, and then supplemented with 400 μL of binding buffer. Finally, a flow cytometer was used to analyze the apoptosis of the cells.

To understand the subcellular localization of MoO_2 QDs, the fluorescence co-localization imaging experiment was performed. MoO_2 QDs were first mixed with an equivalent fluorescent probe (RhB) to acquire MoO_2 QDs/RhB. Then, the Hep G2 cells pre-cultured in Petri dishes were incubated with 200 μg mL^{-1} MoO_2 QDs/RhB for 8 h. After washing with PBS, the cells were co-stained with different organelle-specific trackers (Lyso-Tracker Green, Mito-Tracker Green and ER-Tracker Blue-White DPX). Finally, the cells were washed and fixed by 4% paraformaldehyde for 10 min, and observed under a fluorescence microscope.

Results and discussion

Synthesis and characterization of molybdenum oxide quantum dots

Molybdenum oxide nanomaterials were synthesized *via* a typical light-controlled strategy (Fig. 1a and b). $Mo(CO)_6$ was first heated in dimethyl formamide (DMF) at 80 °C for 1 h to get the yellow intermediate (Y), which has been characterized as

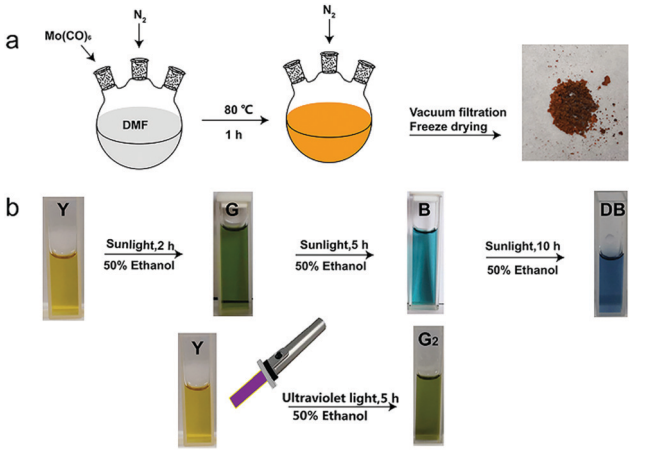

Fig. 1 Schematic illustration of the synthesis process of MoO_x QDs. (a) Synthesis of yellow reduced molybdenum. (b) Synthesis of three molybdenum oxides with different degrees of oxidation.

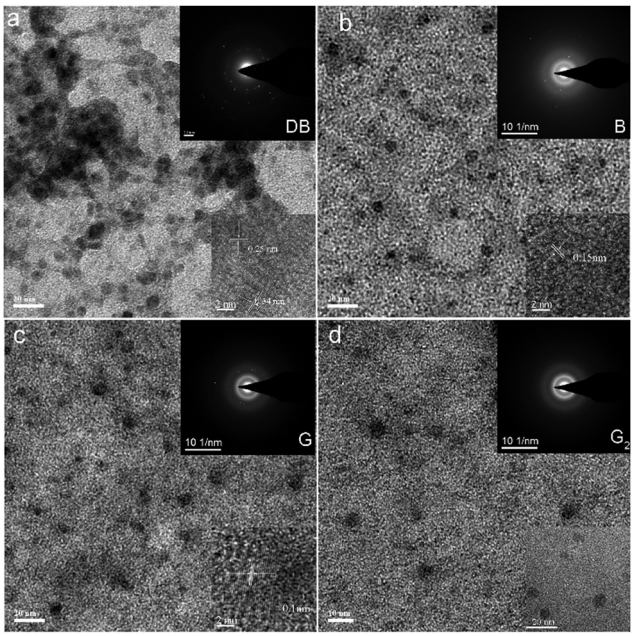

Fig. 2 TEM images of (a) DB, (b) B, (c) G and (d) G_2, respectively. The upper insets show the corresponding selected area electron diffraction (SAED) patterns, and the lower insets display the HRTEM images of the nanostructures.

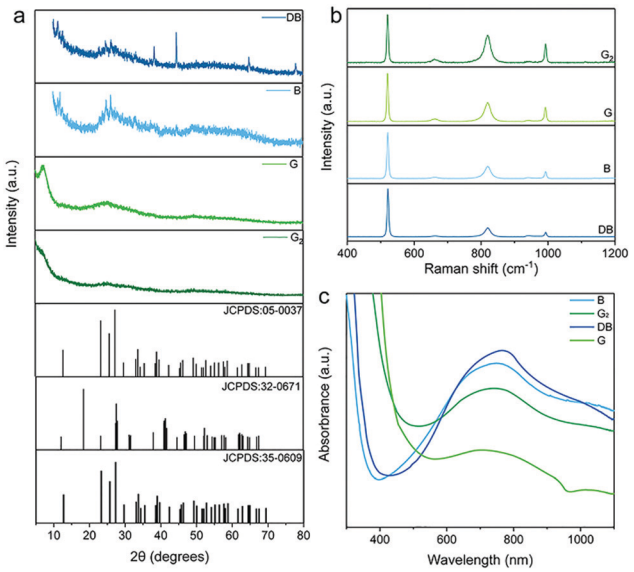

Fig. 3 (a) XRD analysis of G, B, DB and G_2. Black lines correspond to standard patterns of Mo_4O_{11} (JCPDS No. 05-0508), MoO_3 (JCPDS No. 35-0609) and MoO_2 (JCPDS No. 32-0671), respectively. (b) Raman analysis of G, B, DB, and G_2. (c) UV-Vis-NIR absorption spectra of MoO_x QDs at the same Mo concentration of 0.5 mg mL^{-1}.

elementary Mo (Fig. S1 and S2, ESI†). Then, MoO_x QDs in different oxidation states were obtained under sunlight or ultraviolet (UV) irradiation. Significant color changes were observed under sunlight, and the color of the solution changed from yellow to green (G), blue-green (B) and dark blue (DB), respectively. On the other hand, the yellow intermediate became only green (G_2) under UV irradiation, and the color did not change as the radiation time increased.

Transmission electron microscopy (TEM) and high resolution TEM (HRTEM) were used to evaluate the dimensions and crystal structures of the samples. As shown in Fig. 2a–d, four kinds of molybdenum oxides form in the shapes of quantum dots with the sizes of 3–5 nm. The HRTEM image in the lower inset in Fig. 2a reveals that the lattice fringes of DB are 0.25 nm and 0.34 nm, which can be indexed to the (111) and (200) facets of monoclinic MoO_2, respectively.[29,30] The corresponding selected area electron diffraction (SAED) pattern presented in the upper inset also shows an obvious crystal structure. In addition, the lattice fringes of B and G are 0.15 nm and 0.1 nm, respectively (Fig. 2b and c). G2 has no lattice fringes, which may be ascribed to the lattice structural destruction caused by UV light. The amorphous structure of G2 can also be confirmed by the SAED pattern (Fig. 2d).

The as-prepared molybdenum oxide nanomaterials were further studied by X-ray diffraction (XRD) analysis. As shown in Fig. 3a, obvious sharp peaks can be observed in the XRD patterns of DB and B, indicating that DB and B have good crystal structures. The crystal structure of G can also be proved by the peak (7.1°) emerging in the XRD pattern. However, no peaks are observed in the XRD pattern of G_2. According to the standard patterns, there are three typical peaks at 38.4, 44.5, and 64.9 degrees in the XRD pattern of DB, which matches with MoO_2 (JCPDS No. 32-0671). Similarly, B is MoO_3 (JCPDS No. 35-0609) and the others (G_2 and G) are Mo_4O_{11} (JCPDS No. 05-0037). The Raman spectra of MoO_x QDs are shown in Fig. 3b, where the typical peaks of MoO_x QDs at 993 and 820 cm^{-1} can be attributed to the stretching vibration of terminal oxygen (Mo═O) and double coordinated bringing oxygen (Mo_2═O), respectively.[31,32] And the intensities of these two peaks increase gradually from DB to G_2, which means an increasing oxygen content of molybdenum oxide. The optical property was recorded by using UV-Vis-NIR absorption spectroscopy. As shown in Fig. 3c, G, B and DB reveal strong light absorption across visible and NIR regions, which is in keeping with the earlier theories based on Mie-Gan's calculations.[33,34] This excellent optical property indicates the promising potential of MoO_x QDs as potent photothermal nanoagents for PTT.

In order to determine the chemical composition and valence state in the MoO_x nanostructure, X-ray photoelectron spectroscopy (XPS) was used. Fig. 4a shows the Mo, O, and C elements in the XPS spectra of the Mo-based samples, where the characteristic peaks of MoO_x can be observed, such as 231.1 (Mo 3d), 397.1 (Mo $3p_{3/2}$), 415.1 (Mo $3p_{1/2}$), 531.1 (O 1s), and 974.1 eV (Mo(A).[32] The signals of the oxidation state of various Mo species in the MoO_x QD samples are divided into six bands, namely Mo^{4+} $3d_{5/2}$, Mo^{4+} $3d_{3/2}$, Mo^{5+} $3d_{5/2}$, Mo^{5+} $3d_{3/2}$, Mo^{6+} $3d_{5/2}$ and Mo^{6+} $3d_{3/2}$, respectively. Fig. 4b shows the high-resolution XPS spectrum of G, where the binding energies at 231.13 and 234.23 eV are in accordance with Mo^{5+} $3d_{5/2}$ and $Mo^{5+}3d_{3/2}$ of MoO_x, respectively.[34] The peaks at 232.18 and 235.38 eV are separate traits of Mo^{6+} $3d_{5/2}$ and Mo^{6+} $3d_{3/2}$.[36] Calculated on the basis of area ratios of Mo species derived from XPS spectra, the content is 35.25%, 26.20%, 24.34% and

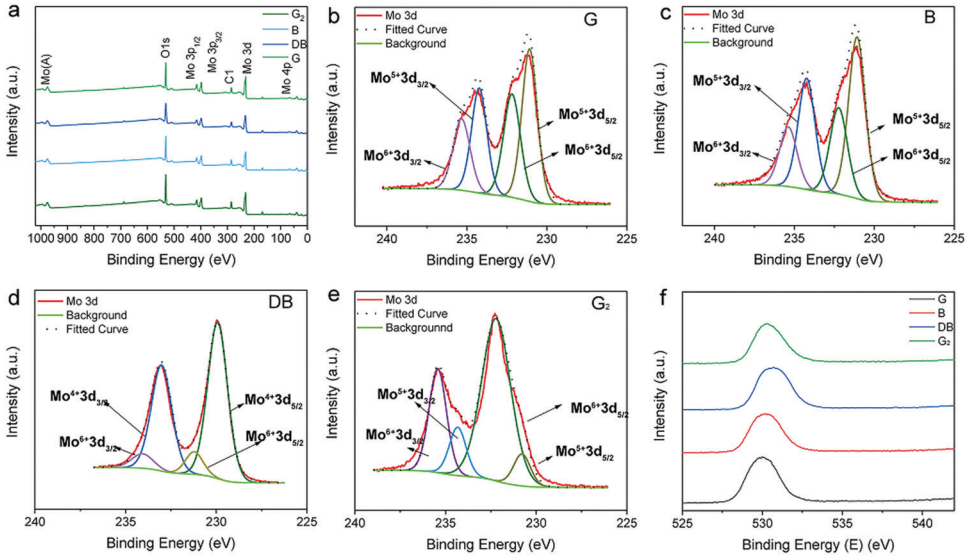

Fig. 4 (a) XPS spectra and (b–e) the high-resolution XPS spectra of Mo 3d in G, B, DB and G_2, respectively. (f) XPS spectra of O 2p in MoO_x QDs.

15.80% for Mo^{5+} $3d_{5/2}$, Mo^{6+} $3d_{5/2}$, Mo^{5+} $3d_{3/2}$ and Mo^{6+} $3d_{3/2}$, respectively, certifying that a large percentage of Mo element existed in a reduction state. As displayed in Fig. 4c, the binding energies at 231.08 and 234.23 eV correspond separately to Mo^{5+} $3d_{5/2}$ and Mo^{5+} $3d_{3/2}$.[35] The peaks at 232.18 and 235.38 eV are in accordance with Mo^{6+} $3d_{5/2}$ and Mo^{6+} $3d_{3/2}$. The atom contents were concluded to be 40.16%, 21.66%, 27.73% and 13.34% for Mo^{5+} $3d_{5/2}$, Mo^{6+} $3d_{5/2}$, Mo^{5+} $3d_{3/2}$ and $20Mo^{6+}$ $3d_{3/2}$, respectively.[37,38] Fig. 4d reveals that the initial $3d_{3/2}$ and $3d_{5/2}$ double peak values at 230.1 and 233.2 eV are characteristic of Mo^{4+} oxidation of MoO_2.[39] The energy gap of 3.1 eV between the two doublets is in keeping with an earlier report.[40] As shown in Fig. 4e, the peaks at 230.78 and 234.33 eV are ascribed to Mo^{5+} $3d_{5/2}$ and Mo^{5+} $3d_{3/2}$, respectively. The binding energy at 232.23 and 235.43 eV can be assigned to Mo^{6+} $3d_{5/2}$ and Mo^{6+} $3d_{3/2}$, respectively. By estimating the area ratio of Mo species from XPS spectra, the DB form represents MoO_2, while the others (B, G and G_2) represent MoO_{3-x} forms. The sunlight results in the increase of the Mo^{5+} states, which transforms G into B, further breaking the oxygen bond, forming DB (with abundant Mo^{4+} states).[41] This change from MoO_x to MoO_2 also promotes broad absorption in the Vis-NIR spectral region (Fig. 3c). Fig. 4f shows the XPS spectra of oxygen 2p peaks of all four samples, which shows the O binding energies of G_2, B, DB, and G at 529.98, 530.23, 530.68, and 530.33 eV, respectively.[42]

SERS properties of molybdenum oxide quantum dots

To evaluate the SERS performance of molybdenum oxide quantum dots, we chose the frequently-used methylene blue (MB) molecule as a Raman probe. Fig. 5a exhibits the SERS spectra of MB at the concentration of 10^{-6} M induced by four molybdenum oxide substrates. G displays a relatively low SERS effect on MB (also see Fig. S3, ESI†). With the increase of oxygen defects, the SERS performance of the MoO_x QDs becomes more intense, and it reaches a maximum at the DB stage (*i.e.* MoO_2), which is consistent with the data reported previously.[18] The concentration-dependent SERS activity of MoO_2 is further illustrated in Fig. 5b, where the SERS spectral pattern of MB excited by MoO_2 fits well with the Raman spectrum of pure MB; and four characteristic Raman peaks of MB molecules, R_1 (1625 cm^{-1}), R_2 (1192 cm^{-1}), R_3 (1181 cm^{-1}) and R_4 (774 cm^{-1}), can clearly be detected on the MoO_2 substrate. Fig. 5c displays the quantitative data of the four typical SERS bands, where the changes in the peaks obey a concentration-dependent manner in the concentration range from 1×10^{-3} M to 1×10^{-8} M. The intensities of

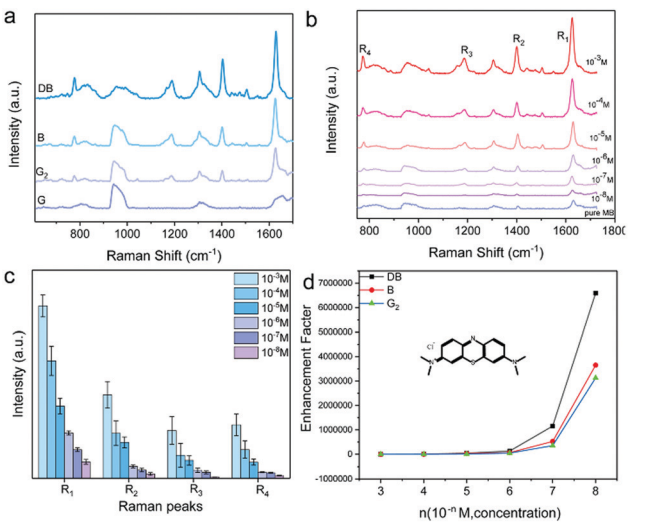

Fig. 5 SERS measurement of MB molecules deposited on MoO_x substrates. (a) SERS spectra of MB molecules (10^{-6} M) deposited on four MoO_x QDs with different oxygen defects. (b) Raman spectra of MB molecules with different concentrations deposited on MoO_2 substrates. (c) The SERS intensities of four typical Raman peaks extracted from the panel. (d) The Raman enhancement factors of MB at different concentrations deposited on various MoO_x substrates.

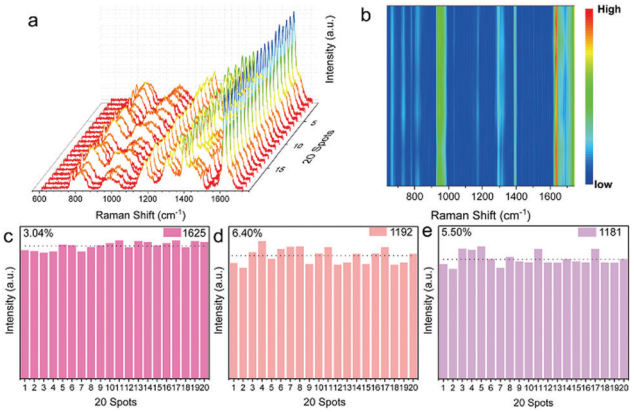

Fig. 6 (a) Repeatability of SERS detection of MB on the same MoO_2 substrate at twenty different sample spots. (b) Uniform pseudo color map of Raman spectra of MB molecules deposited on the MoO_2 substrate. The MB concentration is 10^{-8} M. (c–e) The Raman intensities of the three typical peaks collected from 20 random points on the MoO_2 substrate.

peak R_1 (1625 cm^{-1}, C–C ring vibration) are larger than the other Raman signatures at all concentrations and are used for EF calculation. As displayed in Fig. 5d, the enhancement factors of MB molecules deposited on the three molybdenum oxide substrates increase with decreasing concentration. The Raman enhancement factors of MB molecules deposited on the DB substrate are the biggest among the three molybdenum oxides. The maximum EF for R_1 can be up to 7×10^6 at a concentration of 10^{-8} M. Therefore, the DB colored MoO_x QDs (MoO_2) were used for further investigation.

For the repeatability test, 20 spectral lines randomly collected on the MoO_2 substrate are displayed in Fig. 6a, where highly unified SERS spectral patterns can be observed. We can also notice the uniform color distribution in the corresponding pseudo-color map (Fig. 6b), indicating an excellent SERS repeatability of the MoO_2 QDs. Fig. 6c–e display the relative standard deviations (RSDs) of Raman peaks at 1625 cm^{-1}, 1192 cm^{-1}, and 1181 cm^{-1}, which are 3.04%, 6.40%, and 5.50%, respectively. The good SERS repeatabilities of MB molecules on the MoO_2 substrate at different concentrations can also be seen in Fig. S4 (ESI†). The SERS measurement of malachite green molecules using the MoO_2 substrate was also conducted, which obtained satisfactory results (Fig. S5, ESI†). These results strongly demonstrate that MoO_2 QDs can be used as remarkable SERS substrates with uniform SERS signals.

In addition, MoO_2 was further employed for SERS detection of phenylalanine and amphotericin B, two important bioactive molecules. Phenylalanine is one of the essential amino acids in man, while amphotericin B is a polyene antifungal drug whose residues are harmful to human health. As shown in Fig. 7, the Raman signals of phenylalanine and amphotericin B are significantly enhanced by MoO_2 QDs. There are only two peaks in the normal Raman spectrum of phenylalanine (Fig. 7a). However, more abundant fingerprint information is observed in its SERS counterpart, such as 1024 cm^{-1} (ν_{12}, ring breathing mode), 1157 cm^{-1} (ν_{9a}, C–H bend), 1215 cm^{-1} (symmetric ring-C stretch) and 1611 cm^{-1} (ν_{8a}, C–Cstretch).[43,44] As shown

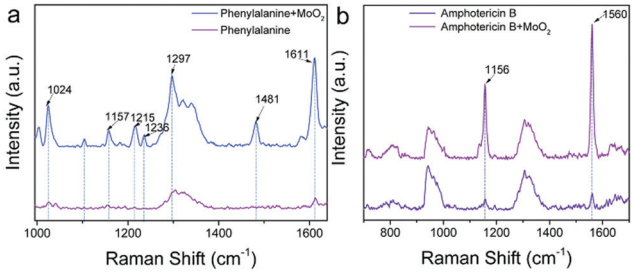

Fig. 7 SERS spectra of (a) phenylalanine (5 mM) and (b) amphotericin B (0.5 mM) deposited on the MoO_2 or silicon wafer substrate.

in Fig. 7a, two obvious Raman bands at 1156 cm^{-1} and 1560 cm^{-1} emerge in the SERS spectrum of amphotericin B, which can be assigned to the C–C stretch, the C–C–H bend and the symmetric C=C stretch, respectively.[45,46] The enhancement factors of phenylalanine (1611 cm^{-1}) and amphotericin B (1559 cm^{-1}) induced by MoO_2 QDs are 1.26×10^4 and 1.37×10^5, which are equivalent to that triggered by noble metal-based SERS substrates, indicating the promising potential of MoO_2 QDs as cheap alternatives for gold or silver for SERS detection. To our knowledge, this is the first time that SERS analysis of biomolecules has been demonstrated using a MoO_x-based semiconductor substrate.

Photothermal ablation of cancer cells based on MoO_x QDs

For photothermal tumor therapeutic application, the photothermal characteristics of MoO_x QDs were investigated. Fig. 8a shows the temperature elevating curves of MoO_2 QD aqueous solutions (100 μg mL^{-1}) under 808 nm laser with the power densities of 0.33, 1 and 2 W cm^{-2} for 600 s, respectively, indicating a good photothermal conversion performance of MoO_2 QDs. A concentration-dependent photothermal heating

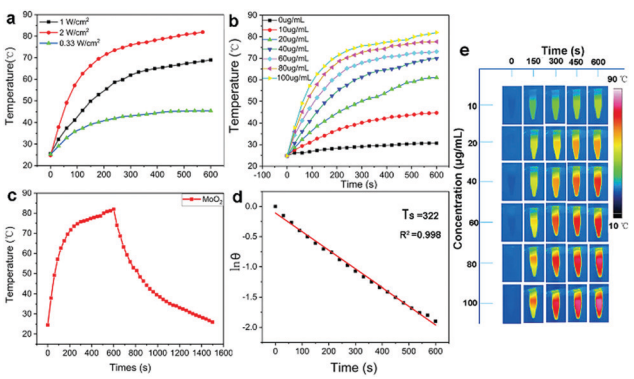

Fig. 8 (a) Temperature heating curves of MoO_2 QD solutions (100 μg mL^{-1}) under 808 nm laser at different power densities. (b) Temperature changes with gradient concentrations (10–100 μg mL^{-1}) of the MoO_2 QD aqueous solutions under irradiation at a wavelength of 808 nm laser with a power density of 2 W cm^{-2} for 600 s. (c) Infrared thermal images of MoO_2 QDs with different concentrations under NIR irradiation. (d) The temperature variation of primary heating and cooling of MoO_2 QDs. (e) The cooling time *vs.* $\ln\theta$ after 808 nm laser irradiation. On the basis of the linear regression analysis, the τ_s value (the slope of the plot) for MoO_2 QDs is determined to be 322 s.

effect of MoO_2 QDs was also noticed (Fig. 8a–c), where the maximal temperature of MoO_2 QD solution under NIR laser irradiation can reach 82 °C, which far exceeds the tolerance of cancer cells. The temperature induced by MoO_2 QDs is much higher than that induced by other kinds of molybdenum oxides (Fig. S6 and S7, ESI†). To quantitatively demonstrate the photothermal feature of MoO_2 QDs, the photothermal transduction efficiency (η) at 808 nm was calculated according to our previous work.[47] As shown in Fig. 8d and e, the sample system time constant (τ_S) was determined to be 322 s, and η is 66.3%, which confirms the outstanding NIR photothermal performance of the molybdenum oxide-based nanostructures. MoO_2 QDs also exhibit good photostability after NIR irradiation, which can be confirmed by the absorption spectrum and TEM observation (Fig. S8, ESI†).

Encouraged by the high photothermal conversion, we then assessed the *in vitro* photothermal efficacy of MoO_2 QDs. In order to improve the stability and biocompatibility of MoO_2 QDs in physiological environments, a layer of calcium carbonate ($CaCO_3$) was coated on the surface of the nanostructures (the characterization of the $CaCO_3$ coating is displayed in Fig. S9, ESI†).[30,48,49] Hep G2 cells were co-cultured with MoO_2 QDs with different concentrations for 12 h, and then the classic MTT assay evaluated the cellular viability. As shown in Fig. 9a, all the cellular viabilities of Hep G2 cells exceed 90%, suggesting that MoO_2 QDs have no apparent toxic effect on Hep G2 cells in the concentration range from 0 to 200 μg mL^{-1}. MoO_2 QDs also show little influence on the normal hepatocytes (Fig. S10, ESI†). We also investigated the subcellular localization of MoO_2 QDs. Hep G2 cells incubated with RhB-labelled MoO_2 QDs were co-stained with different organelle-specific trackers (lysosomes, ER and mitochondria). The data are shown in Fig. 10, where the fluorescence signals ascribable to MoO_2 QDs do not match that of the mitochondria tracker but coincide with that of lysosome and ER probes after 8 h of incubation. For accurate evaluation,

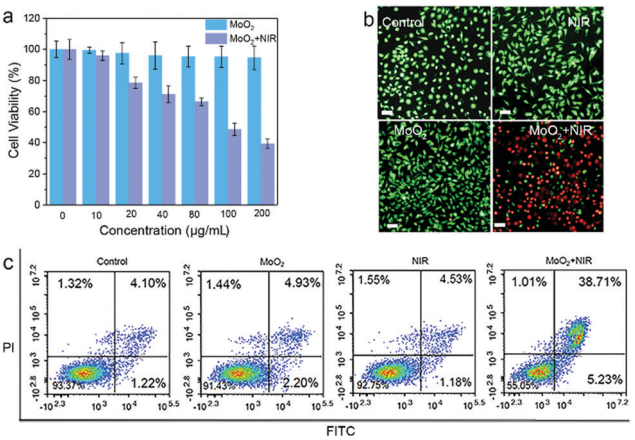

Fig. 9 (a) MTT assay of the cell viabilities of Hep G2 cells treated with different concentrations of MoO_2 QDs under NIR laser irradiation for 2.5 min. The data are represented as mean ± SD of the three independent experiments. (b) Calcein-AM/PI live/dead staining of Hep G2 cells after treatment (scale bar: 100 μm). (c) Flow cytometry analysis of apoptosis in Hep G2 cells after treatment.

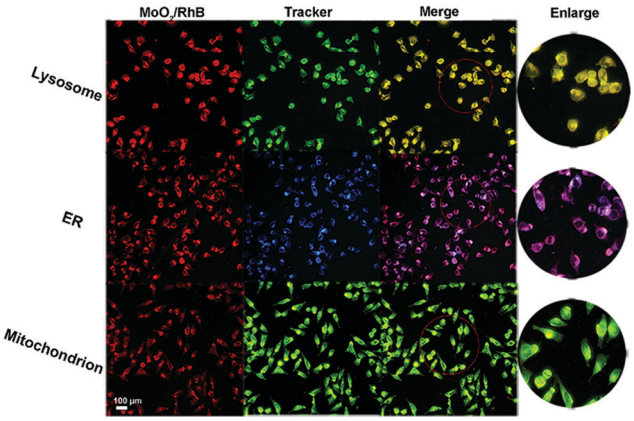

Fig. 10 Fluorescence co-localization analysis of MoO_2 QDs with the ER, lysosome and mitochondria trackers. Scale bar: 100 μm.

the co-localization coefficients are calculated to be 88.5%, 82.0% and 26.6% for lysosomes, ER and mitochondria, respectively, indicating that MoO_2 QDs are mainly distributed in ER and lysosomes (Fig. S11, ESI†).

For the *in vitro* photothermal ablation of cancer cells, Hep G2 cells treated with MoO_2 QDs were exposed to NIR irradiation for 2.5 min. As shown in Fig. 9a, a MoO_2 QD concentration-dependent cellular viability was observed. The tumor inhibition of MoO_2 QDs under NIR laser can achieve 61% when the concentration of nanostructures increases up to 200 μg mL^{-1}, illustrating a good PTT effect. The photothermal tumor ablation performance of MoO_2 QDs was further investigated by calcein AM and propidium iodide (PI) double-staining assay. Fig. 9b displays the fluorescence images of Hep G2 cells after different treatments. Intense and obvious green fluorescence signals can be observed in the cancer cells treated with PBS, NIR and MoO_2 QDs, respectively. In contrast, most of the Hep G2 cells treated with MoO_2 QDs + NIR laser emit red fluorescence, indicating an effective anticancer effect of MoO_2 QDs. In addition, the photothermal treated cancer cells were double-stained with annexinV-FITC and PI for flow cytometry assay. As shown in the four-quadrant flow scatter plots (Fig. 9c), abundant early (5.23%) and late (38.71%) apoptotic cells are observed in the MoO_2 QDs + NIR laser group, while the apoptotic cells in the Control, MoO_2 QD and NIR groups are 5.32%, 7.13%, and 5.71%, respectively. The data described here strongly prove the effective anti-tumor effect *in vitro* using MoO_2 QDs as a novel NIR photothermal nanoagent.

Conclusion

In conclusion, four MoO_x QDs with different oxygen defects have been prepared using a facile and photo-induced strategy. The optical properties of MoO_x QDs are reliant on the oxygen contents in the nanostructures. Among them, MoO_2 QDs with the Mo^{4+} state exhibit optimal NIR optical absorption and SERS activity. The SERS detection limit and maximum EF of MB in solution are 10^{-8} M and 7×10^6, respectively. MoO_2 QDs can also serve as a cheap non-metal SERS substrate to analyze

the fingerprint information of bioactive molecules with an equivalent Raman enhancement compared with traditional nobel metal-based SERS substrates (phenylalanine, EF 1.26×10^4; amphotericin B, EF 1.37×10^5). The strong NIR absorption gives rise to MoO_2 QDs with a high photothermal conversion efficiency of 66.3%. The utilization of MoO_2 QDs as a novel NIR-responsive nanoagent for photothermal tumor therapy *in vitro* has been achieved. The great Raman enhancement and photothermal transduction efficiencies of MoO_2 QDs provide them with potent theranostic potential for oncological diagnosis and treatment.

Conflicts of interest

There are no conflicts of interest to declare.

Acknowledgements

This work is supported by the National Natural Science Foundation of China (11874021, 61675072, 61335011, 81601534 and 21505047), the Science and Technology Project of Guangdong Province of China (2017A020215059), and the Science and Technology Project of Guangzhou City (201904010323).

Notes and references

1 T. Low, A. Chaves, J. D. Caldwell, A. Kumar, N. X. Fang, P. Avouris, T. F. Heinz, F. Guinea, L. Martin-Moreno and F. Koppens, *Nat. Mater.*, 2017, **16**, 182–194.
2 Y. Yan, J. Gong, J. Chen, Z. Zeng, W. Huang, K. Pu, J. Liu and P. Chen, *Adv. Mater.*, 2019, **31**, e1808283.
3 M. Qiu, W. X. Ren, T. Jeong, M. Won, G. Y. Park, D. K. Sang, L. P. Liu, H. Zhang and J. S. Kim, *Chem. Soc. Rev.*, 2018, **47**, 5588–5601.
4 S. Linic, U. Aslam, C. Boerigter and M. Morabito, *Nat. Mater.*, 2015, **14**, 567–576.
5 W. Liu, Q. Xu, W. Cui, C. Zhu and Y. Qi, *Angew. Chem., Int. Ed.*, 2017, **56**, 1600–1604.
6 I. A. de Castro, R. S. Datta, J. Z. Ou, A. Castellanos-Gomez, S. Sriram, T. Daeneke and K. Kalantar-Zadeh, *Adv. Mater.*, 2017, **29**, 1701619.
7 W. Yin, T. Bao, X. Zhang, Q. Gao, J. Yu, X. Dong, L. Yan, Z. Gu and Y. Zhao, *Nanoscale*, 2018, **10**, 1517–1531.
8 W. Liu, X. Li, W. Li, Q. Zhang, H. Bai, J. Li and G. Xi, *Biomaterials*, 2018, **163**, 43–54.
9 R. Li, H. An, W. Huang and Y. He, *Sens. Actuators, B*, 2018, **259**, 59–63.
10 L. Yuan, Y. Niu, R. Li, L. Zheng, Y. Wang, M. Liu, G. Xu, L. Huang and Y. Xu, *J. Mater. Chem. B*, 2018, **6**, 3240–3245.
11 Y. Zhan, Y. Liu, H. Zu, Y. Guo, S. Wu, H. Yang, Z. Liu, B. Lei, J. Zhuang, X. Zhang, D. Huang and C. Hu, *Nanoscale*, 2018, **10**, 5997–6004.
12 D. Cassano, M. Santi, F. D'Autilia, A. K. Mapanao, S. Luin and V. Voliani, *Mater. Horiz.*, 2019, **6**, 531–537.
13 G. Song, J. Hao, C. Liang, T. Liu, M. Gao, L. Chen, J. Hu and Z. Liu, *Angew. Chem., Int. Ed.*, 2016, **55**, 2122–2126.
14 Y. Wang, W. Wang, X. Shen, B. Zhou, T. Chen, Z. Guo, C. Wen, B. Jiang and H. Liang, *ACS Appl. Mater. Interfaces*, 2018, **10**, 42088–42101.
15 A. S. Etman, L. Wang, K. Edström, L. Nyholm and J. Sun, *Adv. Funct. Mater.*, 2019, **29**, 1806699.
16 X. Huang, W. Zhang, G. Guan, G. Song, R. Zou and J. Hu, *Acc. Chem. Res.*, 2017, **50**, 2529–2538.
17 B. Y. Zhang, A. Zavabeti, A. F. Chrimes, F. Haque, L. A. O'Dell, H. Khan, N. Syed, R. Datta, Y. Wang, A. S. R. Chesman, T. Daeneke, K. Kalantar-zadeh and J. Z. Ou, *Adv. Funct. Mater.*, 2018, **28**, 1706006.
18 Q. Zhang, X. Li, Q. Ma, Q. Zhang, H. Bai, W. Yi, J. Liu, J. Han and G. Xi, *Nat. Commun.*, 2017, **8**, 14903.
19 D. Ding, W. Guo, C. Guo, J. Sun, N. Zheng, F. Wang, M. Yan and S. Liu, *Nanoscale*, 2017, **9**, 2020–2029.
20 C. Zong, M. Xu, L. J. Xu, T. Wei, X. Ma, X. S. Zheng, R. Hu and B. Ren, *Chem. Rev.*, 2018, **118**, 4946–4980.
21 X. X. Han, W. Ji, B. Zhao and Y. Ozaki, *Nanoscale*, 2017, **9**, 4847–4861.
22 S. Cong, Y. Yuan., Z. Chen, J. Hou, M. Yang, Y. Su, Y. Zhang, L. Li, Q. Li, F. Geng and Z. Zhao, *Nat. Commun.*, 2015, **6**, 7800.
23 H. Wu, X. Zhou, J. Li, X. Li, B. Li, W. Fei, J. Zhou, J. Yin and W. Guo, *Small*, 2018, **14**, 1802276.
24 H. Li, Q. Xu, X. Wang and W. Liu, *Small*, 2018, **14**, e1801523.
25 Y. Liu, B. Huang and Z. Xie, *Appl. Surf. Sci.*, 2018, **427**, 693–701.
26 Q. Zhang, X. Li, W. Yi, W. Li, H. Bai, J. Liu and G. Xi, *Anal. Chem.*, 2017, **89**, 11765–11771.
27 E. Fazio, A. Speciale, S. Spadaro, M. Bonsignore, F. Cimino, M. Cristani, D. Trombetta, A. Saija and F. Neri, *Colloids Surf., B*, 2018, **170**, 233–241.
28 H. Wu, X. Zhou, J. Li, X. Li, B. Li, W. Fei, J. Zhou, J. Yin and W. Guo, *Small*, 2018, **14**, e1802276.
29 Y. Zhao, Y. Lu, Y. Hu, J.-P. Li, L. Dong, L.-N. Lin and S.-H. Yu, *Small*, 2010, **6**, 2436–2442.
30 Q. Zhang, X. Li, Q. Ma, Q. Zhang, H. Bai, W. Yi, J. Liu, J. Han and G. Xi, *Nat. Commun.*, 2017, **8**, 14903.
31 S. Wang, Q. Gao, Y. Zhang, J. Gao, X. Sun and Y. Tang, *Chem. – Eur. J.*, 2011, **17**, 1465–1472.
32 V. Kalyani, S. Mondal, J. Saha and C. Subramaniam, *Nanoscale*, 2018, **10**, 3663–3672.
33 M. M. Y. A. Alsaif, K. Latham, M. R. Field, D. D. Yao, N. V. Medehkar, G. A. Beane, R. B. Kaner, S. P. Russo, J. Z. Ou and K. Kalantar-zadeh, *Adv. Mater.*, 2014, **26**, 3931–3937.
34 K. Kalantar-zadeh, J. Z. Ou, T. Daeneke, A. Mitchell, T. Sasaki and M. S. Fuhrer, *Appl. Mater. Today*, 2016, **5**, 73–89.
35 M. Chhowalla, H. S. Shin, G. Eda, L.-J. Li, K. P. Loh and H. Zhang, *Nat. Chem.*, 2013, **5**, 263–275.
36 T. A. Tran, K. Krishnamoorthy, Y. W. Song, S. K. Cho and S. J. Kim, *ACS Appl. Mater. Interfaces*, 2014, **6**, 2980–2986.
37 Z. Li, W. Wang, Z. Zhao, X. Liu and P. Song, *RSC Adv.*, 2017, **7**, 28366–28372.
38 P. Qin, G. Fang, W. Ke, F. Cheng, Q. Zheng, J. Wan, H. Lei and X. Zhao, *J. Mater. Chem. A*, 2014, **2**, 2742–2756.
39 T. Schroeder, J. Zegenhagen, N. Magg, B. Immaraporn and H.-J. Freund, *Surf. Sci.*, 2004, **552**, 85–97.

40 D.-R. Hang, K. H. Sharma, C.-H. Chen and S. E. Islam, *Chem. – Eur. J.*, 2016, **22**, 12777–12784.
41 S. Pandey, K. H. Sharma, A. K. Sharma, Y. Nerthigan, D.-R. Hang and H.-F. Wu, *Chem. – Eur. J.*, 2018, **24**, 7417–7427.
42 K. Inzani, M. Nematollahi, F. Vullum-Bruer, T. Grande, T. W. Reenaas and S. M. Selbach, *Phys. Chem. Chem. Phys.*, 2017, **19**, 9232–9245.
43 M. Holecek, *Nutrition*, 2010, **26**, 482–490.
44 S. P. A. Fodor, R. A. Copeland, C. A. Grygon and T. G. Spiro, *J. Am. Chem. Soc.*, 1989, **111**, 5509–5518.
45 M. Gagos, M. Arczewska and W. I. Gruzecki, *J. Phys. Chem. B*, 2011, **115**, 5032–5036.
46 F. Madzharova, Z. Heiner and J. Kneipp, *J. Phys. Chem. C*, 2017, **121**, 1235–1242.
47 Z. Liu, H. Chen, Y. Jia, W. Zhang, H. Zhao, W. Fan, W. Zhang, H. Zhong, Y. Ni and Z. Guo, *Nanoscale*, 2018, **10**, 18795–18804.
48 Y. Zhao, Z. Luo, M. Li, Q. Qu, X. Ma, S.-H. Yu and Y. Zhao, *Angew. Chem., Int. Ed.*, 2015, **54**, 919–922.
49 D. V. Volodkin, R. von Klitzing and H. Moehwald, *Angew. Chem., Int. Ed.*, 2010, **49**, 9258–9261.